

1 Spatiotemporal transcriptomics reveals pathogenesis of viral myocarditis

2 **Authors:** Madhav Mantri¹, Meleana M. Hinchman², David W. McKellar¹, Michael F. Z. Wang¹, Shaun T.
3 Cross^{1,2,3}, John S. L. Parker^{2,3*}, Iwijn De Vlaminc^{1,3*}

4 **Affiliations:** ¹Nancy E. and Peter C. Meinig School of Biomedical Engineering, Cornell University, Ithaca, New
5 York, ²Baker Institute for Animal Health, College of Veterinary Medicine, Cornell University, Ithaca, New York,
6 ³Cornell Institute for Host-Microbe Interactions and Disease, Cornell University, Ithaca, New York.

7
8 *To whom correspondence should be addressed: vlaminc@cornell.edu and jsp7@cornell.edu

9

10 ABSTRACT

11 A significant fraction of sudden death in children and young adults is due to myocarditis, an
12 inflammatory disease of the heart, most often caused by viral infection. Here we used
13 integrated single-cell and spatial transcriptomics to create a high-resolution, spatially resolved
14 map of reovirus-induced myocarditis in neonatal murine hearts. We assayed hearts collected
15 at three timepoints after reovirus infection and studied the temporal, spatial, and cellular
16 heterogeneity of host-virus interactions. We further assayed the intestine, the primary site of
17 reovirus infection to establish a full chronology of molecular events that ultimately lead to
18 myocarditis. We implemented targeted enrichment of viral transcripts to establish the cellular
19 targets of the virus in the intestine and the heart. Our data give insight into the cell-type
20 specificity of innate immune responses, and into the transcriptional states of inflamed cardiac
21 cells that recruit circulating immune cells, including cytotoxic T cells which induce pyroptosis in
22 the myocarditic tissue. Analyses of spatially restricted gene expression in myocarditic regions
23 and the border zone around those regions identified immune-mediated cell-type specific injury
24 and stress responses. Overall, we observe a dynamic and complex network of cellular
25 phenotypes and cell-cell interactions associated with viral myocarditis.

26

27

28

29 INTRODUCTION

30 Viral infection is the most common cause of myocarditis^{1,2}. The resulting inflammatory
31 cardiomyopathy can lead to arrhythmias, dilated cardiomyopathy, and death^{1,3,4}. In humans,
32 viral myocarditis is challenging to study because of the low sensitivity of available diagnostic
33 testing, the acute onset of the disease, the focal nature of the disease, and the extreme
34 heterogeneity of immune-virus interactions in complex cardiac tissues⁴⁻⁶. In mice, mammalian
35 orthoreovirus offers a flexible model system⁷. After oral inoculation, the Type 1 Lang (T1L)
36 reovirus strain initially infects the gastrointestinal tract. Within days the infection then spreads
37 to secondary sites in the body, including the heart, leading to myocarditis in up to 50% of
38 infections⁷⁻⁹. Yet, even in this mouse model, the molecular pathogenesis of viral myocarditis is
39 difficult to study because of the complex network of cardiac and immune cell types involved
40 and the cellular, spatial, and temporal heterogeneity of the disease^{2,10}. Consequently, neither
41 the cell types that are responsible for the innate immune response, nor the cell types that are
42 infected *in vivo* have been identified. Similarly, the responses of infected and uninfected
43 bystander cells within the heart have not been characterized. In addition, the protective versus
44 damaging effects of adaptive immune responses have not been quantified. Experiments in
45 mice with severe combined immunodeficiency (SCID) indicate that adaptive immune
46 responses are not required for myocardial injury and heart failure^{7,11}, but these observations do
47 not exclude the possibility that immune-cell-mediated injury is important in immunocompetent
48 mice. Unbiased characterization of all cellular phenotypes as a function of time and location
49 within infected cardiac tissues is needed to address these knowledge gaps.

50 Here we used integrated single-cell and spatially resolved RNA-sequencing (RNA-seq) to
51 study the cellular and spatial heterogeneity of myocarditic processes in the hearts of reovirus-
52 infected neonatal mice at multiple time points after infection. We also applied these
53 technologies to study the innate response to reovirus infection in the intestine. In addition, we
54 performed time-series single-cell RNA-seq (scRNA-seq) of cardiac tissues of mice infected
55 with a reovirus point mutant that does not cause myocarditis. To establish viral tropism, we
56 implemented molecular enrichment of non-polyadenylated viral transcripts that were otherwise
57 poorly represented in the transcriptomes. Our measurements give insight into the cardiac cell-
58 type specificity of innate immune responses, into the tropism of the virus in the intestine and
59 the heart, and into the transcriptional states of cell types involved in the production of
60 inflammatory cytokines and the recruitment of circulating immune cells. Analyses of spatially
61 restricted gene expression in myocarditic regions and the border zone around those regions
62 identified injury and stress responses in different cell types, including cardiomyocytes. Overall,
63 our data identify spatially restricted cellular interactions and cell-type specific host responses
64 during reovirus-induced myocarditis.

65

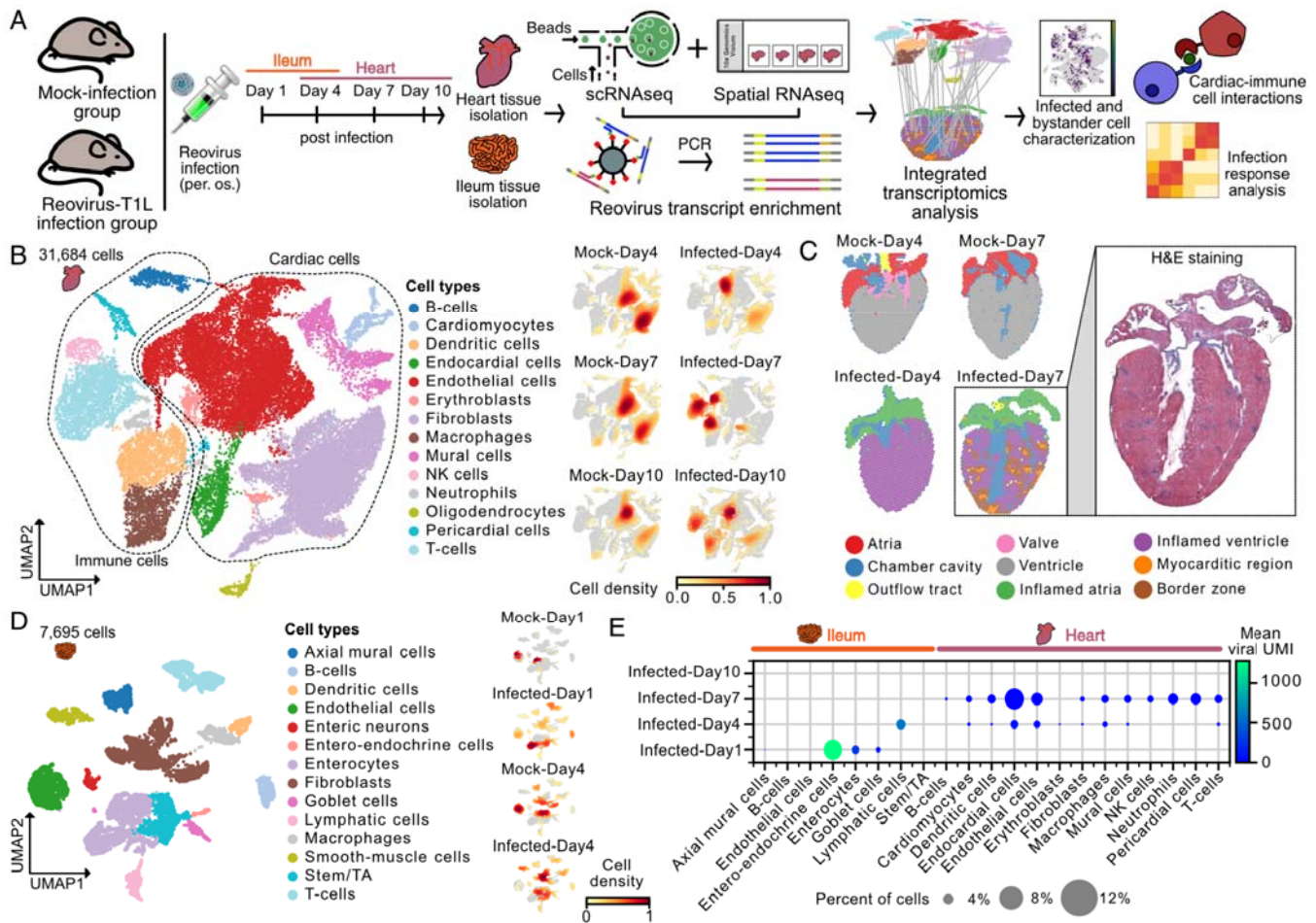
66

67 RESULTS

68 Single-cell and spatial transcriptomics of reovirus T1L-infected neonatal mice hearts

69 To elucidate the pathogenesis of reovirus-induced myocarditis, we analyzed heart tissues
70 collected from neonatal mice infected orally with either the T1L strain of reovirus or a mock
71 control (**Methods, Fig. 1A**). We generated scRNA-seq data for 31,684 cells from infected
72 hearts and mock controls at 4, 7, and 10 days post-infection (dpi), and 8,243 spatial
73 transcriptomes for four tissue sections from infected hearts and mock controls at 4 and 7 dpi
74 from the same litter (10x Chromium and 10x Visium, **Methods, Supp Fig. 1A-1B and Fig. 1B-**
75 **1C**). The single-cell transcriptomes represented 18 distinct cell types, including
76 cardiomyocytes, endocardial cells, cardiac fibroblasts, endothelial cells, mural cells,
77 macrophages, neutrophils, NK cells, dendritic cells, T cells, and B cells (**Methods, Fig 1B,**
78 **Supp Fig 1C-E**). Clustering of the spatial transcriptomic data revealed distinct transcriptional
79 programs for myocarditic regions and the border zone surrounding the myocarditic regions in
80 the 7 dpi reovirus-infected heart that corresponded to areas of tissue damage identified by
81 H&E staining (**Fig. 1C**). The combination of scRNA-seq and spatial transcriptomics allowed us
82 to resolve and visualize cell types and gene expression in a spatial context (**Supp Fig 1F**).
83 Because the virus first infects the gastrointestinal tract before it spreads to other body sites
84 including the heart, we also performed scRNA-seq and spatial transcriptomics on ileum. We
85 obtained 7,695 single-cell transcriptomes and 8,027 spatial spot transcriptomes for ileum from
86 mock and infected samples at 1 and 4 dpi (**Fig. 1D, Supp Fig. 2A-C**).

87 To faithfully identify reovirus transcripts in the ileum and heart, which are not polyadenylated,
88 we performed hybridization-based enrichment of viral fragments captured in the scRNA-seq
89 libraries (**Methods**). We used the viral transcript data from empty droplets to threshold ambient
90 viral transcript contamination and accurately characterize infected cells (**Methods**). In the
91 ileum, we captured a total of 13,100 unique viral transcripts, with viral load decreasing from 1
92 dpi to 4 dpi (**Supp Fig. 2D-2E**). At 1 dpi, entero-endocrine cells had the highest fraction of
93 infected cells followed by enterocytes and goblet cells, all of which are present in the gut
94 epithelium. Lymphatic endothelial cells were infected at 4 dpi, suggesting that the virus
95 reaches the bloodstream via lymphatic drainage to allow transmission of the virus to secondary
96 sites in the body, including the heart, as shown before¹² (**Supp Fig. 2E**). We captured 2,762
97 unique viral transcripts from 392 cells in the T1L-infected hearts. The viral load first increased
98 from 4 dpi to 7 dpi and then decreased from 7 dpi to 10 dpi, consistent with viral titer assays
99 performed on whole hearts^{9,13} (**Fig. 1E, Supp Fig. 2F-2G**). Endocardial and endothelial cells
100 were the most frequently infected cell types at 4 dpi, suggesting that endocardial cells lining
101 the ventricular lumen and endothelial cells lining the cardiac vasculature are among the first
102 cells to be infected in the heart (**Fig. 1E**). We detected viral transcripts in neutrophils, dendritic
103 cells, and T cells in the 7 dpi heart (**Fig. 1E**). This observation suggests that antigen-
104 presenting cells and immune cells may contribute to the spread of infection to other organs in
105 the body. The role of infected dendritic cells in bringing more reovirus to the cardiac tissue
106 during systemic infection has been discussed previously⁸.



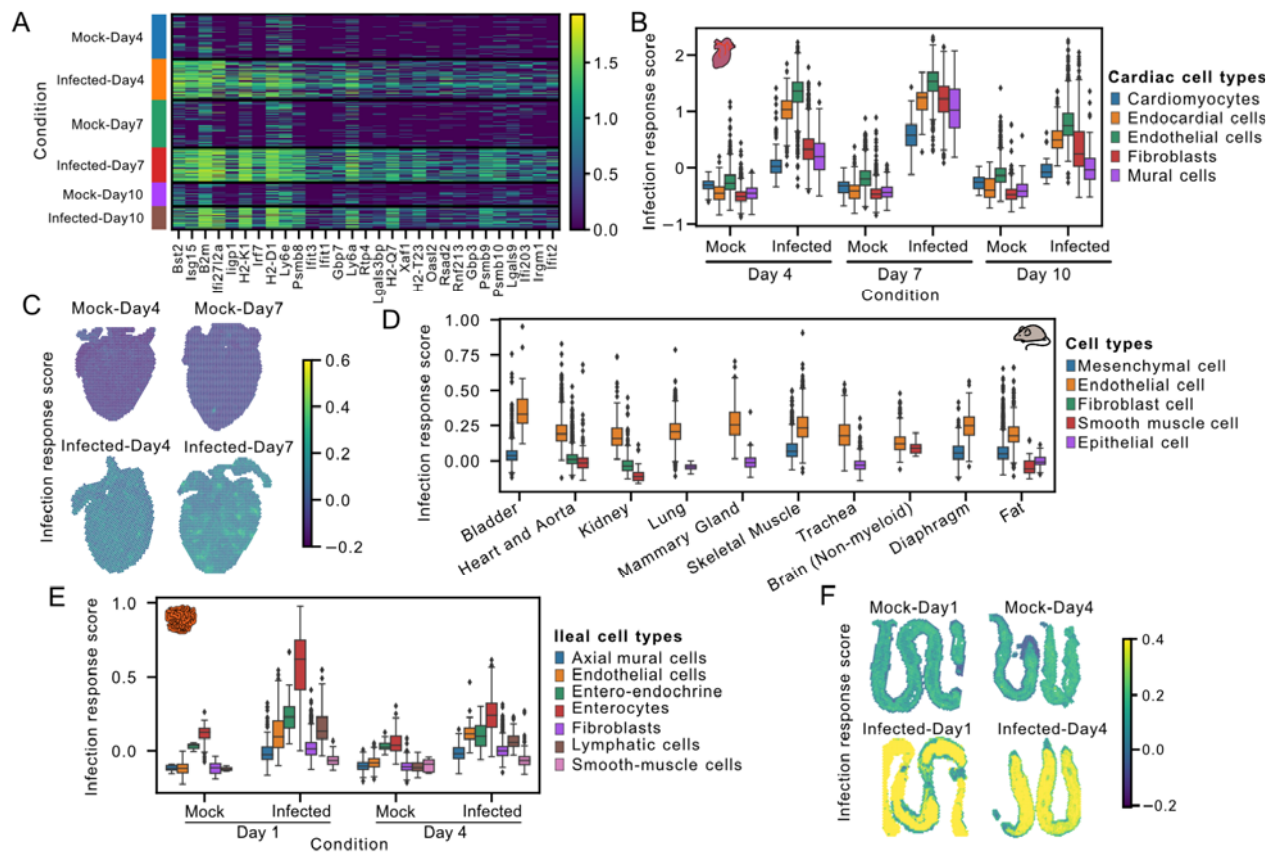
107
108 **Figure 1: Single-cell and spatial transcriptomics of cardiac tissue from reovirus infected neonatal mice. A)**
109 Experiment and analysis workflow. **B)** UMAP projection of 31,684 single-cell transcriptomes from mock-infected
110 and reovirus-infected hearts at 4, 7, and 10 dpi, clustered by gene expression and colored by cell type (left).
111 UMAP plots showing the gaussian kernel density of cells across samples for the heart scRNA-seq data (right). **C)**
112 8,243 spatial transcriptomes of cardiac tissue sections from mock-infected and reovirus-infected mice pups at 4
113 and 7 dpi. Haematoxylin and eosin (H&E) stained image of reovirus-infected myocarditic tissue section used for
114 spatial transcriptomics at 7 dpi (in box). **D)** UMAP projection of 7,695 single-cell transcriptomes from mock-
115 infected and reovirus-infected ileum at day 1 and 4 dpi, clustered and colored by cell type (left). UMAP plots
116 showing the gaussian kernel density of cells across samples for the ileum scRNA-seq data (right). **E)** Dot plot
117 showing the percent of cells with non-zero viral transcripts and the mean viral transcript counts (UMIs) in ileal and
118 cardiac cell types.

119 **Endothelial cells are primed with basal interferon response and play an important role**
120 **in initiating host innate immune response**

121 To detect early transcriptional differences in the cardiac tissue after infection, we performed
122 Differential Gene Expression Analysis (DGEA, mock vs infected hearts at 4 dpi, **Methods**).
123 This analysis revealed a significant upregulation of 226 genes in the infected heart (two-sided
124 Wilcoxon test, log fold-change > 1.0 and p-value < 0.01), including genes related to the
125 interferon- β pathway, interferon signaling, and innate immune responses (**Supp Fig 3A-3B,**
126 **Fig. 2A**).

127 To quantify and compare the overall magnitude of early infection responses across different
128 cell types, we computed a gene module score (infection response score, IR, module of 226
129 genes selected above). Comparison of the IR of different cell types in absence of infection
130 revealed a small, but higher IR in endothelial cells as compared to other cardiac cell types
131 (**Fig. 2B**). In response to infection, an increase in IR was observed for all cardiac cell types,
132 but the greatest increase in IR was observed for endothelial cells (**Fig. 2B**). These data
133 suggest that endothelial cells lining the cardiac vasculature are important initiators of the host
134 defense to viral infection. Comparison of IR scores using the spatial transcriptomic data shows
135 increased IR scores in the infected hearts at 4 and 7 dpi with the highest scores found in
136 myocarditic regions (**Fig. 2C**). Given our observation that endothelial cells within the heart had
137 the highest IR score in absence of infection, we asked if this observation was unique to heart
138 tissue or was a more general phenomenon. To this end, we used the Tabula Muris scRNA-seq
139 mouse atlas¹⁴ and estimated the IR of ~16,000 cells of five major cell types (epithelial cells,
140 fibroblasts, endothelial cells, smooth muscle cells, and mesenchymal cells) across 10 different
141 organs and tissues. This analysis revealed that endothelial cells consistently had the highest
142 IR score across all tissues in mice (**Fig. 2D**). These results indicate that endothelial cells lining
143 the vasculature have a higher basal expression of innate response genes within most tissues,
144 which may prime these cells to respond to viral dissemination within the blood and lymphatics.

145 To investigate the cell-type-specific IR in the ileum, the primary site of reovirus infection, we
146 performed DGEA on reovirus-infected at 1 dpi compared to mock-infected ileal cells and found
147 a significant upregulation of 438 genes (two-sided Wilcoxon test, log fold-change > 1.0 and p-
148 value < 0.01), related to the interferon-beta pathway, interferon signaling, and innate immune
149 responses (**Supp Fig. 3C-3D**). We computed an IR score using this module of 438 genes and
150 observed higher basal IR scores in enterocytes and entero-endocrine cells as compared to
151 other ileal cell types (**Fig. 2E**). Enterocytes further showed the highest increase in IR score
152 after infection, followed by entero-endocrine, endothelial, and lymphatic cells (**Fig. 2E**).
153 Comparison of IR scores for spatial transcriptomic data further supported our analysis of the
154 scRNA-seq data, showing increased IR scores in the infected ileum at 1 and 4 dpi with the
155 highest scores evident within intestinal mucosa and villi (**Fig. 2F**). The intestinal epithelial cells
156 must tolerate commensal microorganisms present in the lumen of the gut and yet still be
157 responsive to invasive pathogens. Our data suggest that to achieve this, enterocytes and
158 entero-endocrine cells in the gut epithelium are primed with a basal interferon response and
159 play an important part in mounting innate immune responses in the early stages of viral
160 infection.



161
 162 **Figure 2: Endothelial cells have the highest basal interferon response and the highest increase in innate**
 163 **response upon reovirus infection** **A)** Heatmap showing the expression of the 25 most upregulated genes in the
 164 reovirus-infected heart as compared to mock at 4 dpi. **B)** Infection response score for cardiac cell types in scRNA-
 165 seq data across mock-infected and reovirus-infected hearts at three distinct stages. The infection response score
 166 represents the gene module score for a panel of 226 genes significantly upregulated (two-sided Wilcoxon test, log
 167 fold-change > 1.0 and p-value < 0.01) in the reovirus-infected sample as compared to the mock-infected sample
 168 at 4 dpi. **C)** Infection response score (defined above) across spots in spatial transcriptomics data. **D)** Infection
 169 response score calculated for five common cell types across 13 tissues from tabula-muris mouse atlas data. **E)**
 170 Infection response score for ileum cell types in scRNA-seq data across mock-infected and reovirus-infected ileum
 171 at two distinct stages. The infection response score represents the gene module score for a panel of 438 genes
 172 significantly upregulated (two-sided Wilcoxon test, log fold-change > 1.0 and p-value < 0.01) in the reovirus-
 173 infected ileum sample as compared to the mock-infected sample at 1 dpi. **F)** Infection response score (defined
 174 above) for spatial transcriptomics data from mock-infected and reovirus-infected ileum at two distinct stages.

175 **Cytotoxic T cells recruited by inflamed endothelial cells induce pyroptosis**

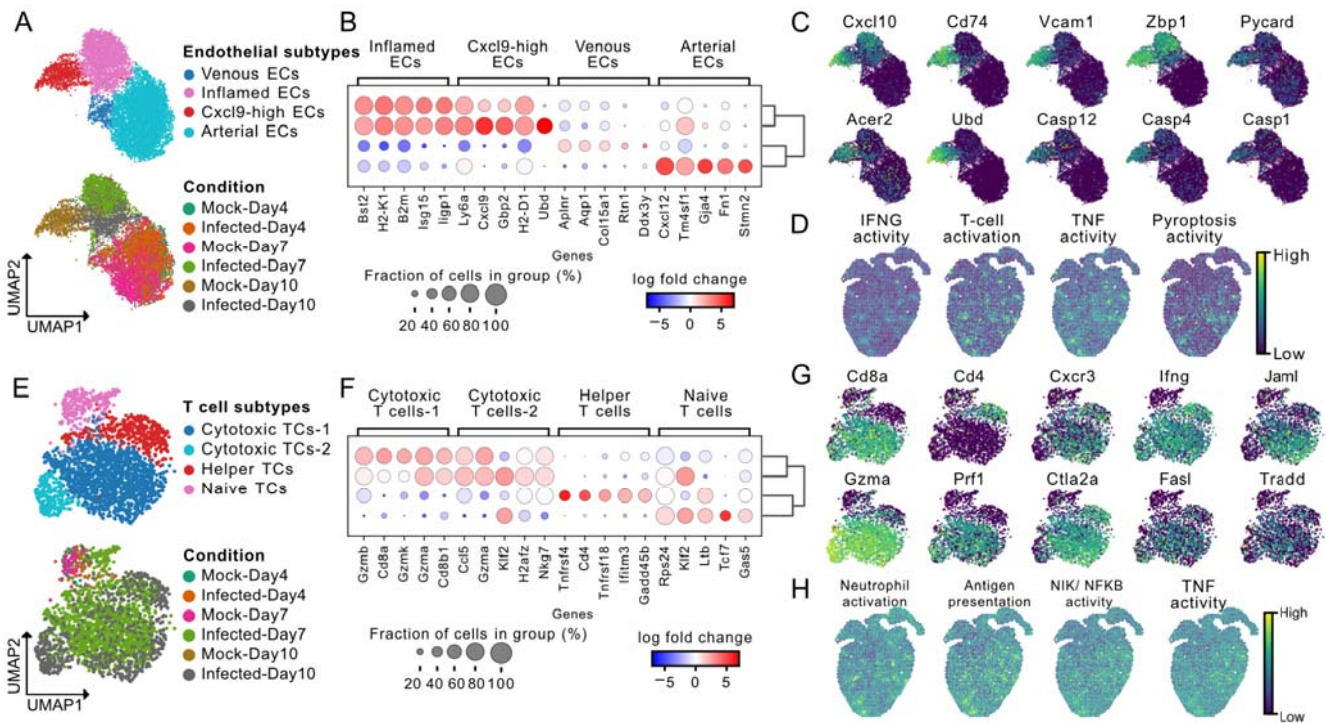
176 To explore the heterogeneity of endothelial cell phenotypes in more detail, we reclustered all
 177 9,786 cardiac endothelial cells in the scRNA-seq data. We observed four distinct phenotypes:
 178 **i)** uninfamed venous endothelial cells expressing *Nr2f2* and *Ap1nr* mainly derived from the
 179 mock controls, **ii)** arterial endothelial cells expressing *Gja4*, *Gja5*, and *Cxcl12* derived from
 180 both mock and infected cardiac hearts, **iii)** inflamed endothelial cells derived from infected
 181 hearts at 4 and 10 dpi, and **iv)** inflamed endothelial cells from the heart at 7 dpi, with both
 182 inflamed endothelial cell clusters expressing *Isg15*, *ligp1*, and *Ly6a* (**Fig. 3A-B**). DGEA across
 183 endothelial subclusters revealed that the inflamed 7 dpi endothelial cells overexpressed
 184 chemokines *Cxcl9* and *Cxcl10*, which are generally involved in immunoregulatory and

185 inflammatory processes, but more specifically in the recruitment of T cells (**Fig. 3B-3C, Supp**
186 **Fig. 3E**). In line with this observation, T cells in the 7 dpi hearts expressed the *Cxcr3* receptor
187 (see below). The *Cxcl9*-high inflamed endothelial cells furthermore expressed high levels of
188 cell adhesion marker genes *Vcam1* and *Icam1*, which help immune cells in the blood to attach
189 to endothelial cells¹⁵ (**Fig. 3C, Supp Fig. 3E, 3I**). The endothelial cells also overexpressed
190 MHC class 1 (*H2-D1* and *H2-K1*) and MHC class 2 (*Cd74*) molecules, suggesting their
191 involvement in antigen presentation to adaptive immune cells (**Fig. 3B-C, Supp Fig. 3E**).
192 Endothelial cells have been shown to be involved in antigen presentation and shaping the
193 cellular immune response in infectious myocarditis¹⁵. Gene ontology (GO) term enrichment
194 analysis identified pathways further supporting the *Cxcl9*-high endothelial cells' involvement in
195 leukocyte cell-cell adhesion, T cell activation, regulation of interleukin-8 production, and
196 response to cytokines, interferon-gamma, interleukin-1, and tumor necrosis factors (**Supp Fig.**
197 **3F**).

198 The observation that endothelial cells are involved in the recruitment of T cells prompted us to
199 explore the heterogeneity of T cells in the infected hearts in more detail. To this end, we
200 reclustered 2,205 T cell single-cell transcriptomes, leading to four subclusters representing
201 three T cell subtypes, *i*) *Cd8+* cytotoxic T cells, *ii*) *Cd4+* helper T cells, and *iii*) naive T cells
202 (**Fig 3E-F**). Both the cytotoxic and helper T cells identified within infected hearts expressed
203 *Cxcr3* receptor, interferon-gamma (*Ifn γ*), and the chemokines *Ccl3*, *Ccl4*, *Ccl5*, *S100A4*, and
204 *S100A6*, suggesting their involvement in neutrophil recruitment and activation (**Fig. 3G, Supp**
205 **Fig. 3G**). The *Cxcr3* receptor binds selectively to the chemokines *Cxcl9* and *Cxcl10*, promoting
206 chemotaxis (**Fig. 3G**). Cytotoxic T cells represented the majority of infiltrating T cells and
207 expressed *Prf1*, *Gzma*, *Gzmb*, and *Gzmk*, coding for lytic molecules associated with the
208 granzyme-dependent exocytosis pathway¹⁶ (**Fig. 3F-G, Supp Fig. 3G, 3K**). These cells also
209 expressed tumor necrosis factor superfamily genes *Fasl* and *Tradd*, which are involved in the
210 Fas-induced cell death pathway. *Fasl* binds to *Fas* on the surface of target cells and mediates
211 programmed cell death signaling and NF- κ B activation (**Fig. 3G**). The *Fasl*-*Fas* apoptosis
212 pathway is important in regulating T cells, in promoting tolerance to self-antigens, and is a
213 mechanism by which cytotoxic T cells kill target cells¹⁶. GO enrichment analysis identified
214 pathways involved in neutrophil activation and degranulation, processing and presentation of
215 exogenous peptide antigen, interleukin-1-mediated signaling pathway, tumor necrosis factor-
216 mediated signaling, NIK/NF-kappaB signaling, cellular response to lectin, and apoptotic
217 processes (**Supp Fig. 3H**).

218 The downstream gene markers for cell death-associated pathways *Pycard*, *Acer2*, *Zbp1*, and
219 Caspases *Casp1*, *Casp4*, and *Casp12* were enriched in the *Cxcl9*-high endothelial cells. This
220 raises the possibility that cytotoxic lymphocytes are responsible for inflamed endothelial cell
221 death (**Fig. 3B-3C, Supp Fig. 3I**). GO enrichment of endothelial cells confirmed upregulation
222 of cell death pathways including activation of cysteine-type endopeptidase activity involved in
223 the apoptotic process, positive regulation of extrinsic apoptotic signaling pathway, and
224 pyroptosis pathway (**Supp Fig. 3F**). We assessed the spatial transcriptomic data to validate

225 direct interactions between *Cxcl9*-high inflamed endothelial cells and T cells and found that
 226 they were indeed spatially co-localized in the myocarditic regions and the border zone (**Supp**
 227 **Fig. 1F**). We calculated gene module scores for genes associated with ontology terms
 228 enriched in *Cxcl9*-high endothelial and cytotoxic T cells for spatial transcriptomics data and
 229 found these pathways to be enriched in the myocarditic regions (**Fig. 3D, 3H, and Supp Fig.**
 230 **3I-3L**). Collectively, these results suggest that endothelial cells lining the cardiac vasculature
 231 act as a blood-heart barrier and play an important role in the recruitment and activation of the
 232 host adaptive immune system. These cells may be the target of both direct viral damage and
 233 immune-mediated damage during reovirus-induced myocarditis. Damage to the
 234 microvasculature within the heart may then cause loss of blood supply and be a factor in the
 235 subsequent death of cardiomyocytes independent of direct viral replication.



236

237 **Figure 3 Cytotoxic T cells recruited by inflamed endothelial cells induce pyroptosis in myocarditic tissue**
 238 **A)** UMAP projection of 9,786 single-cell endothelial cell transcriptomes from mock-infected and reovirus-infected
 239 hearts at 4, 7, and 10 dpi colored by endothelial cell (EC) subtype clusters (phenotypes) (top) and condition
 240 (bottom). **B)** Heatmap showing top-five differentially expressed genes (two-sided Wilcoxon test, log fold-change >
 241 1.0 and p-value < 0.01) for endothelial cell subtypes. **C)** UMAP plot showing the expression of genes upregulated
 242 in *Cxcl9*-high endothelial cells. **D)** Spatial transcriptomics maps of cardiac tissue from reovirus infected hearts at 7
 243 dpi showing gene module scores calculated for four GO terms enriched in *Cxcl9*-high endothelial cells. **E)** UMAP
 244 projection of 2,205 single-cell T cell (TC) transcriptomes from mock-infected and reovirus-infected hearts at 4, 7,
 245 and 10 dpi colored by T cell subtype clusters (top) and condition (bottom). **F)** Heatmap showing top-five
 246 differentially expressed genes (two-sided Wilcoxon test, log fold-change > 1.0 and p-value < 0.01) for T cell
 247 subtypes. **G)** UMAP plot showing the expression of genes upregulated in cytotoxic T cells from myocarditic heart
 248 at 7 dpi. **H)** Spatial transcriptomics maps of cardiac tissue from reovirus infected hearts at 7 dpi showing gene
 249 module scores calculated for four GO terms enriched in cytotoxic T cells from myocarditic heart.

250

251 **Spatially restricted gene expression in myocarditic tissue**

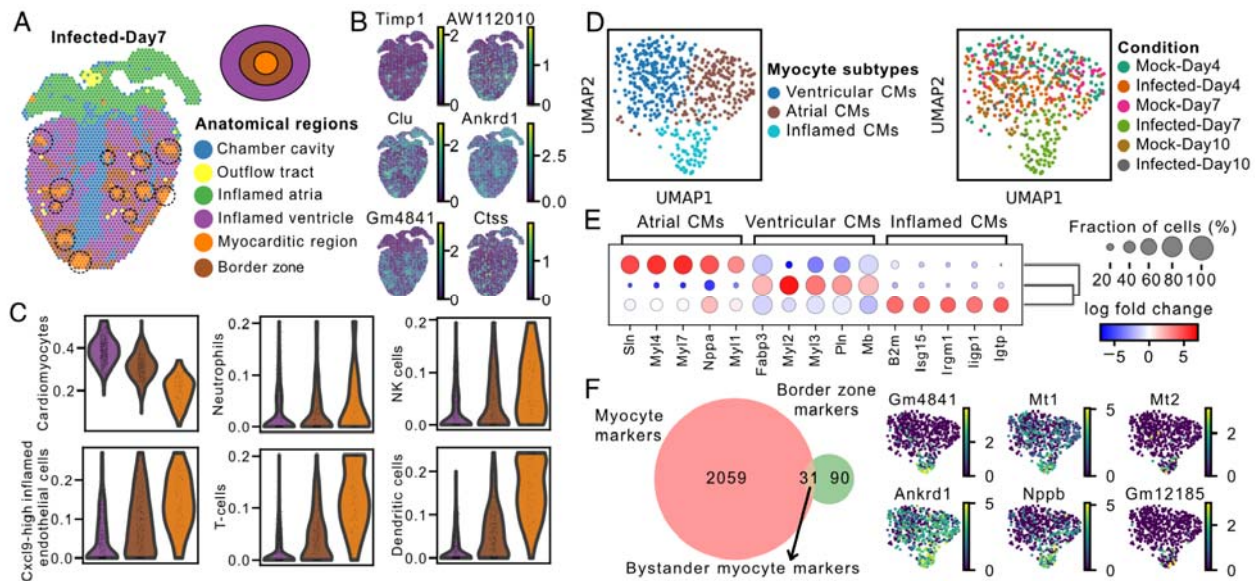
252 The spatially restricted nature of myocarditis motivated us to explore the spatial heterogeneity
253 of gene expression in reovirus-infected hearts. Our initial clustering of the spatial
254 transcriptomic data revealed distinct transcriptional programs for myocarditic regions, the
255 tissue bordering these myocarditic regions, and the rest of the ventricular tissue (**Fig. 1C, 4A**).
256 Differential spatial gene expression analysis for these regions revealed upregulation in the
257 myocarditic regions of cell-type markers for infiltrating immune cells, (*Cd8a* and *Gzma* for T
258 cells, *Nkg7* for NK cells, *S100a8* for neutrophils), markers of inflammation (*Cd52* and *Lyc62*,
259 **Supp Fig. 4A**), and chemokines and cytokines (*Ccl5*, *Ccl2*, *Cxcl9*, and *Cxcl10*). Analysis of the
260 corresponding scRNA-seq data showed that *Ccl5* is expressed by dendritic cells, *Ccl2* by
261 fibroblasts, and *Cxcl9* and *Cxcl10* by endothelial cells. The receptor for *Ccl2*, *Ccr2*, is
262 expressed in macrophages, indicating that fibroblasts use the *Ccl2-Ccr2* axis for macrophage
263 recruitment during myocardial inflammation, as described recently^{17,18} (**Supp Fig. 4A-B**).
264 Collectively these analyses show that chemokine-producing endothelial and cytokine-
265 producing fibroblast cells recruit immune cells to the myocarditic tissue.

266 Closer inspection of the myocarditic regions and border zones showed an upregulation of
267 additional genes of interest, including *Timp1*, *AW112010*, *Clu*, *Ankrd1*, *Gm4841*, and *Ctss*
268 (**Fig. 4B**). *Timp1* is mainly expressed by inflamed fibroblasts in the scRNA-seq data (**Supp**
269 **Fig. 4D**). *Timp1* is a natural inhibitor of the matrix metalloproteinases (MMPs), a group of
270 peptidases involved in the degradation of the extracellular matrix. Upregulation of *Timp1* in
271 patients with deteriorating heart failure was reported previously¹⁹. *AW112010* is expressed by
272 inflamed endothelial cells and fibroblasts in the scRNA-seq data and was previously found to
273 code for an interferon-induced small secreted protein with a crucial role in the innate immune
274 response to infection and inflammation²⁰. *Clu* is expressed in a subset of inflamed cells from all
275 cardiac cell types in our data and was previously shown to be upregulated during severe
276 myocarditis²¹ (**Supp Fig. 4D**). *Ctss*, expressed mainly in monocytes, encodes a protease used
277 for degradation of antigenic proteins to peptides for presentation on MHC class II molecules.
278 Increased formation of immunoproteasomes in susceptible mice has been shown to affect the
279 generation of antigenic peptides and the subsequent T cell activity in viral myocarditis^{22,23}. GO
280 term analysis of genes upregulated in the border zone revealed enrichment of terms related to
281 the response to tumor necrosis factor, response to interleukin-1, and NIK/ NF- κ B signaling
282 (**Supp Fig. 4E**).

283 To further understand the effect of immune cell infiltration on the cell type composition around
284 the myocarditic regions, we assessed cell type proportions as a function of distance from
285 myocarditic regions in the tissue. We quantified the cell type proportions in myocarditic
286 regions, the border zones, and the rest of the ventricular tissue, and found that the fraction of
287 *Cxcl9*-high endothelial cells, *Ccl2*+ fibroblasts, T cells, dendritic cells, and NK cells was
288 increased in the myocarditic regions, and the fraction of cardiomyocytes was reduced in
289 myocarditic regions (**Fig. 4C, Supp Fig. 1F**). To understand the phenotype of *Ccl2*+ fibroblasts
290 enriched in myocarditic region and border zone, we reclustered 9,192 fibroblast cells from the

291 scRNA-seq dataset and identified a distinct cluster of inflamed *Ccl2*+ fibroblasts from the
292 infected heart at 7 dpi (**Supp. Fig. 4G-4H**). The *Ccl2*+ fibroblast cells expressed high levels of
293 MHC class 1 (*H2-D1* and *H2-K1*), adhesion marker genes *Vcam1* and *Icam1*, and other genes
294 like *Serpina3g*, *C3*, and *Ms4a4d* (**Supp Fig. 4I**). Moreover, these fibroblast cells also
295 expressed *Casp1* and *Casp4*, suggesting pyroptosis activity in response to cytotoxic T cells
296 (**Supp Fig. 4I**).

297 To investigate the effect of inflammation on cardiomyocytes in myocarditic hearts, we
298 reclustered 502 cardiomyocyte cells from the scRNA-seq dataset and identified three distinct
299 phenotypes: *i*) ventricular myocytes expressing *Myl2*, *Myl3*, and *Mb* derived from mock and
300 infected hearts at 4 and 10 dpi, *ii*) atrial myocytes expressing markers *Myl4*, *Myl7*, and *Nppa*
301 derived from mock and infected hearts at 4 and 10 dpi, and *iii*) inflamed myocytes from the
302 infected heart at 7 dpi expressing innate immunity genes *Isg15*, *Igtp*, and *ligp1* (**Fig. 4D-E**).
303 Inflamed myocytes from the infected heart at 7 dpi had a distinct phenotype as compared to
304 the myocytes from hearts at 4 and 10 dpi, which clustered with myocyte cells from mock-
305 infected hearts (**Fig. 4E**). To find transcriptional signatures for myocytes present in the border
306 zone, we selected genes that were both enriched in cardiomyocyte cells in the scRNA-seq
307 data and upregulated in the border zone. This analysis revealed that cardiomyocytes in the
308 border zone expressed *Gm4841*, *Gm12185*, *Mt1*, *Mt2*, *Ankrd1*, and *Nppb* (**Fig. 4F, Supp Fig.**
309 **4F**). *Gm4841* and *Gm12185* are interferon-inducible genes produced in response to interferon-
310 gamma. *Mt1* and *Mt2* genes modulate inflammation and support remodeling in ischemic
311 cardiomyopathy in mice²⁴. Upregulation of *Ankrd1*, a myocyte survival factor, occurs during
312 late-stage heart disease in patients with idiopathic dilated cardiomyopathy²⁵. A recent study
313 shows that cardiomyocytes expressing *Ankrd1* are localized in the border zone on day 1 post-
314 myocardial infarction²⁶. Together, our analysis reveals that tissue injury is localized to
315 myocarditic regions with remodeling programs being active in the border zone and
316 demonstrates the importance of spatially resolved molecular measurements to study viral
317 myocarditis.

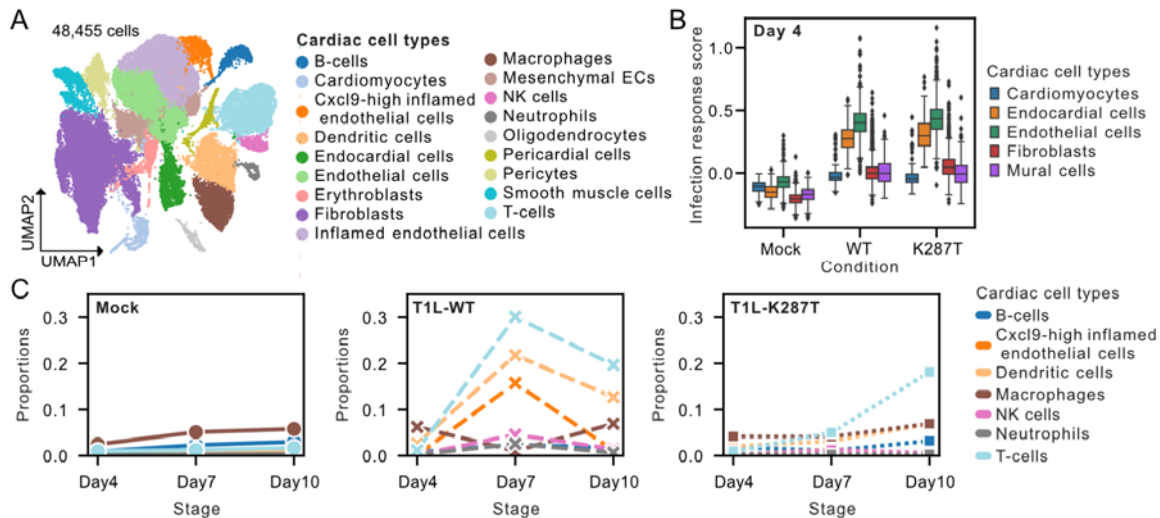


318
319 **Figure 4 Myocarditic regions and the border zone have distinct transcriptomic profiles and cell type**
320 **specific signatures.** **A)** Spatial transcriptomics map of cardiac tissue sections from reovirus-infected mice pups
321 at 7 dpi colored by spot clusters representing transcriptionally distinct tissue regions. **B)** Spatial transcriptomics
322 maps of cardiac tissue sections from reovirus-infected mice pups at day 7 showing the expression of differentially
323 expressed genes of interest in the myocarditic and the border zone. **C)** Changes in average predicted cell-type
324 proportions across the infected ventricle, for cell types enriched in the myocarditic region and the border zone. **D)**
325 UMAP projection of 502 single-cell cardiomyocyte cell transcriptomes from mock-infected and reovirus-infected
326 hearts at 4, 7, and 10 dpi colored by myocyte cell subtype clusters (phenotypes) (left) and condition (right). **E)**
327 Heatmap showing top-five differentially expressed genes (two-sided Wilcoxon test, log fold-change > 1.0 and p-
328 value < 0.01) for cardiomyocyte cell subtypes. **F)** Venn Diagram showing myocyte-specific genes upregulated in
329 the border zone around the myocarditic regions (left). UMAP plot showing the expression of myocyte-specific
330 genes which are upregulated in the border zone of myocarditic regions (right).

331 **Reduced adaptive immune cell infiltration associated with reovirus K287T mutant**

332 We recently reported a reovirus mutant T1L S4-K287T (K287T) which has a point mutation in
333 the S4 gene encoding outer capsid protein sigma-3 (σ_3), a double-stranded (ds) RNA-binding
334 multifunctional protein that promotes viral protein synthesis and facilitates viral entry and
335 assembly⁹. K287T successfully infects the heart but produces lower viral titers relative to
336 reovirus wild-type (WT) and does not cause myocarditis⁹. To validate our findings, we
337 performed additional scRNA-seq for K287T infected hearts at 4, 7, and 10 dpi. We generated a
338 total of 16,771 single-cell transcriptomes and integrated the data with the data from the wild-
339 type (WT) virus. K287T-infected cells clustered with WT infected cells for almost all cell types
340 (**Fig. 5A, Supp Fig. 4J**). We performed viral transcript enrichment and compared the mean
341 viral transcripts in WT and mutant infected cells. We found similar levels of viral transcripts for
342 WT and K287T viruses at 4 dpi but a 60-fold lower viral load for K287T at 7 dpi, consistent with
343 viral titer assays⁹ (**Supp Fig. 4K-4L**). We then compared early host responses among cardiac
344 cell types due to K287T and WT infection. K287T induced a similar level of innate immune
345 responses as WT reovirus with endothelial cells showing the highest increase in cardiac IR
346 score (as defined before) at 4 dpi (**Fig. 5B**). We analyzed the cell type composition of *Cxcl9*-
347 high endothelial cells and immune cells between K287T- and WT-infected hearts and found

348 that the 7 dpi K287T-infected heart at 7 dpi had significantly fewer *Cxcl9*-high endothelial cells
 349 and immune cells infiltrating the heart compared to WT-infected heart. These differences are in
 350 line with the reduced levels of inflammation and tissue injury related to the K287T mutant (**Fig.**
 351 **5C**). Our results show that cardiac endothelial cells mount a potent and robust innate immune
 352 response even when infected with the K287T mutant virus with reduced replication in most cell
 353 types. Clearance of the virus from the infected cells by 7 dpi and a weaker adaptive host
 354 response then leads to the non-myocarditic phenotype of mutant K287T-infected hearts.



355 **Figure 5 A robust innate immune response but reduced adaptive immune cell infiltration explains the non-**
 356 **myocarditic phenotype on infection with reovirus K287T mutant. A)** UMAP projection of 48,455 single-cell
 357 cell transcriptomes from mock-infected, reovirus-wildtype (WT) infected, and reovirus mutant (K287T) infected
 358 hearts at 4, 7, and 10 dpi colored by cell-type clusters. **B)** Infection response score for cardiac cell types in
 359 scRNA-seq data across mock-infected, reovirus-WT infected, and reovirus-K287T infected hearts on 4 dpi. The
 360 infection response score represents the gene module score for a panel of 226 genes significantly upregulated in
 361 the reovirus-WT infected sample as compared to the mock-infected sample at 4 dpi. **C)** Changes in cell-type
 362 proportions with time for cell types detected in the myocarditic regions. Panels show the changes in cell-type
 363 proportions across mock-infected, reovirus-WT infected, and reovirus-K287T infected cells.

365 DISCUSSION

366 Viral myocarditis has been recognized as a cause of heart failure for more than 50 years, but it
 367 is still a challenging disease to study, diagnose, and treat²⁷. Here, we used integrated spatial
 368 and single-cell RNA-seq to dissect the temporal, spatial, and cellular heterogeneity of reovirus-
 369 induced acute myocarditis in a neonatal mouse model. We assayed ileum and heart tissues at
 370 multiple time points after infection. We investigated the cell types that are infected, and the
 371 cellular and spatial heterogeneity of innate and adaptive immune responses. We generated a
 372 total of thirteen scRNA-seq and eight spatial transcriptomics datasets, spanning two organs,
 373 four time points, and three infection conditions. Our data provide detailed insight into the
 374 chronology of molecular events that lead to reovirus-induced myocarditis. After oral
 375 inoculation, reovirus T1L infects entero-endocrine and enterocyte cells in the gut epithelium
 376 within 1 dpi. These cells mount a potent innate immune response to inhibit viral replication.
 377 The virus then infects the gut lymphatic cells within 4 dpi and through lymphatic drainage, the

378 virus is transmitted via the bloodstream to secondary sites in the body, including the heart.
379 Around 4 dpi, the virus infects the endothelial cells lining the cardiac vasculature. Endothelial
380 cells mount a potent innate immune response in the heart. In symptomatic cases, inflamed
381 endothelial cells secrete chemokines to recruit circulating immune cells, including cytotoxic T
382 cells. Tissue-infiltrating cytotoxic T cells then induce pyroptosis in the myocarditic tissue.
383 Overall, our experiments reveal a dynamic and spatially heterogeneous network of cellular
384 phenotypes and cell-cell interactions associated with reovirus-induced myocarditis.

385 Integrated high-throughput scRNA-seq and spatial transcriptomics was recently used to study
386 heart development^{31,32} and heart disease^{26,33}, but these methods have not been used to study
387 viral myocarditis prior to our work. Bulk RNA-seq has been used previously to profile
388 transcriptomic signatures of infection, inflammation, and tissue injury associated with viral
389 myocarditis^{9,28,29}. Yet, these ensemble-level approaches do not capture the cellular and spatial
390 heterogeneity of host response to infection. scRNA-seq has recently been used to study
391 Coxsackievirus B3 (CVB3)-induced myocarditis in a mouse model³⁰. Lasrado et al. report
392 inflammatory phenotypes of myeloid cells, the role of fibroblasts in remodeling and
393 inflammation, and the role of cytotoxic T-cells in CVB3-induced myocarditis. However, the
394 cardiac cell types that are targeted by the virus, the cell type heterogeneity in basal interferon
395 response and innate immune response, and spatially restricted transcriptional programs in
396 myocarditic tissue and border zone were not explored in the study.

397 Previous studies have claimed that the direct cytopathic effect of viral replication on cardiac
398 cells is the main cause of cardiac damage during reovirus-induced myocarditis^{7,34}. Notably,
399 Sherry et al. found that reovirus infection can induce myocarditis in immunodeficient mice
400 lacking B and/or T cells, suggesting that reovirus-induced myocarditis does not strictly require
401 adaptive immunity^{7,11}. However, these previous experiments do not rule out the possibility that
402 the host adaptive immune response can augment or delimit the nature and amount of host
403 damage in immune-competent mouse, as is suggested by our work. Holm et al. and Stewart et
404 al. have studied the protective role of innate immune responses in reovirus-induced
405 myocarditis^{13,35}. However, the temporal, spatial, and cell type heterogeneity of basal type-I IFN
406 and innate immune responses to infection had not been characterized before our work.
407 Miyamoto et al. and Stewart et al. compared basal levels of type-I IFN between cardiac
408 myocytes and fibroblasts *in vitro* but these studies did not include all the cell types that make
409 up complex cardiac tissues^{36,37}.

410 Spatiotemporal characterization of viral myocarditis is crucial to understanding the viral and
411 host factors that are important for disease pathology. This knowledge may ultimately lead to
412 novel diagnostic approaches and better treatments. Several viruses that frequently infect
413 humans can cause myocarditis, including Adenovirus, enteroviruses, Epstein-Barr virus,
414 human Herpesvirus 6, parvovirus B19, and SARS-CoV2. The approaches that we have
415 implemented here can be used in future studies to investigate how the induction,
416 pathophysiology, and course of myocarditis induced by these viruses differs. We hope that the

417 data and analysis routines that we make available here will be a valuable resource for such
418 future studies.

419

420

421

422

423

424 **METHODS**

425 **Reovirus infections of neonatal C57BL/6J mice.**

426 Confirmed pregnant female C57BL/6J mice were ordered from Jackson Laboratories to be
427 delivered at embryonic stage E14.5. Litters weighing 3 gram/ pup were gavaged using
428 intramedic tubing (Becton Dickinson 427401) per os with 50 μ l with 10^7 PFU reovirus type 1
429 lang (T1L): wildtype or K287T mutant in 1x phosphate buffered saline (PBS) containing green
430 food color (McCormick) via a 1ml tuberculin slip tip syringe (BD 309659) and 30G x 1/2 needle
431 (BD 305106). Litters treated with 1x PBS containing green food color alone on the same day
432 were used as mock controls for the respective infection groups. The mock-infected and
433 reovirus-infected mice pups were weighed daily until the time points used in the study (days 1,
434 4, 7, and 10). All animal work was conducted ethically, conforming to the U.S. Public Health
435 Service policy, and was approved by the Institutional Animal Care and Use Committee at
436 Cornell University (IACUC Number 2019-0129).

437 **Sample preparation for single-cell transcriptomics of cardiac tissue.**

438 We sacrificed mock-infected and reovirus-infected C57BL/6J mice on day 4, day 7, and day 10
439 post-infection and collected cardiac tissues for single cell transcriptomics. Hearts from
440 respective stages were isolated aseptically, washed with ice-cold Hank's Balanced Salt
441 Solution, HBSS (with calcium and magnesium chloride; Gibco 14025-134), and minced into 1-
442 2mm pieces. Cardiac tissue pieces were then digested in tissue dissociation media with
443 200U/mL collagenase type II (Gibco 17100-015), 1 mg/ml dispase (Sigma D4693), and 3mM
444 calcium chloride in HBSS for four cycles of 10 minutes under mild agitation at 37°C in 1.5 ml
445 eppendorf tubes. After every 10-minute cycle, cell suspension was collected, added to ice-cold
446 1x PBS with 0.04% bovine serum albumin (BSA; Sigma A3803) and new dissociation media
447 was added to the tubes. At the end of the digestion, the cells were passed through a 70 μ m
448 filter and centrifuged into a pellet. To remove most blood contaminants, samples were
449 resuspended in an ammonium-chloride-potassium (ACK) lysis buffer (Lonza #10-548E) for 3-5
450 minutes and centrifuged. Samples were then washed again in PBS with 0.04% BSA and then

451 resuspended at 1×10^6 cells per ml. Cells from each sample were stained with Trypan Blue
452 and cell viability was calculated on an automated cell counter (Countess II) before loading the
453 cells on 10x Chromium. We used these cell viabilities to adjust the number of cells loaded on
454 10x Chromium to get the desired number of transcriptomes from viable cells for each sample
455 (5000 cells per sample).

456 **Sample preparation for single-cell transcriptomics of intestinal tissue.**

457 We sacrificed mock-infected and reovirus-infected C57BL/6J mice on days 1 and 4 post-
458 infection and collected intestinal ileum tissue for single cell transcriptomics. Intestinal ileum
459 from respective stages were isolated aseptically, washed with ice-cold Hank's Balanced Salt
460 Solution, HBSS (without calcium and magnesium chloride; Gibco 14175-095) to remove
461 contamination. The ileum tissue was then opened longitudinally, washed again with HBSS,
462 and minced into 1-2mm pieces. To isolate the epithelial layer of cells, ileum tissue pieces were
463 incubated in HBSS with 10mM Ethylenediaminetetraacetic acid (EDTA, Invitrogen 15575-038)
464 and 1mM Dithiothreitol, (DTT, Sigma 43816-10ML) for two cycles of 10 minutes under mild
465 agitation at 37°C. After every 10-minute cycle, cell suspension containing the intestinal
466 epithelial cells was collected, added to ice-cold 1x PBS with 0.04% bovine serum albumin
467 (BSA; Sigma A3803). The undigested pieces of lamina propria were then washed thoroughly
468 with PBS (with calcium and magnesium chloride; Gibco 14080-055) to get rid of all EDTA.
469 These pieces were then transferred to fresh tubes and incubated in 200U/ml Collagenase type
470 I (Gibco 17100-017) and 3mM calcium chloride in PBS for three cycles of 10 minutes under
471 mild agitation at 37°C in 1.5 ml eppendorf tubes. After every 10-minute cycle, cell suspension
472 containing the lamina propria cells was collected, added to ice-cold phosphate buffered saline,
473 PBS with 0.04% BSA in separate tubes. At the end of the digestion, the cells were passed
474 through a 40µm filter and washed twice in PBS with 0.04% BSA and then resuspended at
475 1×10^6 cells per ml. Cells from intestinal epithelium and lamina propria for each sample were
476 stained with Trypan Blue and cell viability was calculated on automated cell counters
477 (Countess II). Cell counts adjusted with viability were then pooled as 40% epithelial cells and
478 60% lamina propria to adjust the number of cells loaded on 10x Chromium and to get the
479 desired number of transcriptomes from viable cells for each sample (5000 cells per sample).

480 **Single-cell RNA sequencing library preparation.**

481 5000-6000 viable cells per sample (for heart and ileum tissues) were targeted on the
482 Chromium platform (10x Genomics) using one lane per sample per time point. Single-cell
483 libraries were built using the Chromium Next GEM Single Cell 3' Library Construction V3 Kit
484 (10x Genomics) and were then sequenced on an Illumina NextSeq 500 using 75 cycle high
485 output kits (Index 1= 8, Read 1=28, and Read 2=55) for all samples. Sequencing data
486 were aligned to a combined mouse and reovirus reference genome (described below) using
487 the Cell Ranger 6.0.0 pipeline (10x Genomics).

488 **Sample preparation for Visium spatial transcriptomics.**

489 Whole hearts and intestinal ileum were isolated using aseptic techniques and placed in ice
490 cold sterile Hank's Balanced Salt Solution, HBSS (without calcium and magnesium chloride;
491 Gibco 14175-095). Blood and other contamination were carefully removed by perfusing the
492 tissues with fresh HBSS. Fresh tissues were immediately embedded in Optimal Cutting
493 Compound (OCT) media (SAKURA 25608-930) and frozen in a liquid-nitrogen-cooled
494 isopentane (EMD Millipore, MX0760) bath for spatial transcriptomics experiments. The tissue
495 blocks were cut into 10µm sections using Thermo Scientific CryoStar NX50 cryostat and
496 mounted on Visium Gene Expression slides (10x Genomics), which were pre-cooled to -20°C
497 and used for the Visium Spatial Gene Expression experiment.

498 **Visium spatial transcriptomics library preparation.**

499 We used the Visium Spatial Gene Expression (10x Genomics) platform for the spatial
500 transcriptomics experiments. Tissue sections from fresh-frozen hearts (mock-infected and
501 reovirus-infected at day 4 and day 7 post infection) and ileum (mock infected and reovirus
502 infected at day 1 and day 4 post infection) were mounted with one section per capture area on
503 individual Visium Gene Expression slides. These sections are then fixed in pre-chilled
504 methanol for 30 minutes and then hematoxylin and eosin (H&E) stained and imaged, which is
505 later used by the 10x Genomics Space Ranger (version 1.0.0) software to detect the spots
506 which are covered by the tissue. The optimal permeabilization time for 10 µm thick sections
507 was found to be 18 minutes for the heart and 12 minutes for the ileum using the 10x Genomics
508 Visium Tissue Optimization kit. Spatially tagged cDNA libraries were built using the 10x
509 Genomics Visium Spatial Gene Expression 3' Library Construction V1 Kit. H&E-stained heart
510 tissue sections were imaged using Zeiss PALM MicroBeam laser capture microdissection
511 system at 20x objective and the images were stitched and processed using Fiji ImageJ
512 software. cDNA libraries were sequenced on an Illumina NextSeq 500/550 using 150 cycle
513 high output kits (Read 1 = 28, Read 2 = 120, Index 1 = 10, and Index 2 = 10) for ileum
514 and on an Illumina NextSeq 2K (P2 flow cell) using the 100-cycle kit (Read 1 = 28, Read 2 =
515 96, Index 1 = 10, and Index 2 = 10). Fiducial frames around the capture area on the
516 Visium slide were aligned manually and spots covering the tissue were selected using Loop
517 Browser 4.0.0 software (10x Genomics). Sequencing data was then aligned to a combined
518 mouse and reovirus reference genome (described below) using the Space Ranger 1.0.0 (10x
519 Genomics) pipeline to derive a feature spot-barcode expression matrix. Visium slide number
520 V19B23-046 was used for spatial transcriptomics experiment on mice hearts (mock-infected 4
521 dpi: capture area D1, reovirus-infected 4 dpi: capture area B1, mock-infected 7 dpi: capture
522 area C1, and reovirus-infected 7 dpi: capture area A1). Visium slide number V19B23-045 was
523 used for spatial transcriptomics experiment on mice ileum tissue (mock-infected 1 dpi: capture
524 area D1, reovirus-infected 1 dpi: capture area B1, mock-infected 4 dpi: capture area C1, and
525 reovirus-infected 4 dpi: capture area A1).

526 **Hybridization-based enrichment of viral fragments**

527 We performed a hybridization-based enrichment of viral fragments on a part of scRNA-seq
528 libraries using xGen NGS target enrichment kit (IDT; 1080577). In this approach, a panel of 5'-
529 biotinylated oligonucleotides is used for capture and pulldown of target molecules of interest,
530 which are then PCR amplified and sequenced. We designed a panel of 202 biotinylated probes
531 tiled across the entire reovirus T1L genome to selectively sequence viral molecules from the
532 scRNA-seq libraries (**Supp Table 1**). 300ng of fragmented and indexed scRNA-seq libraries
533 from reovirus-WT infected hearts, reovirus-mutant infected hearts, and reovirus-infected ileum
534 were pooled in three separate reactions for xGen hybridization capture. Two rounds of
535 hybridization capture using the xGen enrichment protocol were performed for every reaction to
536 enrich viral transcripts. Amplification was performed for a total of 18 PCR cycles after the first
537 round of capture. 50% of the amplified product was used for the second round of hybridization
538 capture and amplification was performed for a total of 5 PCR cycles after the second round of
539 enrichment. Post-enrichment products were pooled and sequenced on Illumina Mini-seq for
540 ileum libraries and NextSeq 500 for heart libraries.

541 **Reference genome and annotation**

542 *Mus musculus* genome and gene annotations (assembly: GRCm38) were downloaded from
543 the Ensembl genome browser, and reovirus strain type-1 Lang genome and gene annotations
544 were downloaded and compiled from the NCBI browser. We have shared reovirus genome
545 sequence and annotation files on figshare with the identifier
546 <https://doi.org/10.6084/m9.figshare.c.5726372>. Genomes were processed using the Cell
547 Ranger v-3.0.0 (10x Genomics) pipeline's mkref command.

548 **Single-cell RNAseq data processing and visualization**

549 Cells with fewer than 200 unique genes or more than 20 percent of transcripts aligning to
550 mitochondrial genes were removed. The single-cell transcriptomes were log-transformed and
551 normalized using the Scanpy package version-1.8.1³⁸. We used Scanpy to choose the highly
552 variable genes with min_disp=0.5 and max_mean=3 thresholds. We then performed mean
553 centering and scaling while regressing out total UMI counts, percent mitochondrial transcripts,
554 S score, and G2M score, followed by principal component analysis (PCA) to reduce the
555 dimensions of the data to the top 20 principal components (PCs). Uniform Manifold
556 Approximation and Projection (UMAP) and the Nearest Neighbor (NN) graph were initialized in
557 this PCA space using the first 20 PCs. The cells were then clustered using the Leiden method
558 with multiple values of clustering resolution to get fine (resolution=0.5) and broad
559 (resolution=0.3) celltype clusters. Cell-type-specific canonical gene markers along with
560 differentially expressed genes (wilcoxon method) for each cluster were used to assign cell type
561 labels. Normalized gene expression was visualized on DotPlots, UMAP plots, and Violin plots
562 across cell type groups. A few cell type clusters representing cell states of the same cell type
563 were grouped into broad cell type groups using cell type marker genes and then used for
564 downstream analysis. Differential gene expression analysis (DGEA) was performed using the

565 rank_gene_groups function in Scanpy with the Wilcoxon statistical method. All gene module
566 scores were calculated using the score_genes function in scanpy.

567 **Reclustering and analysis of endothelial cells, T cells, fibroblasts, and cardiomyocytes**

568 Normalized gene expression for a specific cell type group was extracted from the combined
569 scRNA-seq dataset. We used Scanpy to reselect the highly variable genes within that cell type
570 group with min_disp=0.5 and max_mean=3 thresholds. We then performed mean centering
571 and scaling while regressing out total UMI counts, percent mitochondrial transcripts, S score,
572 and G2M score, followed by principal component analysis (PCA) to reduce the dimensions of
573 the data to the top 20 principal components (PCs). Uniform Manifold Approximation and
574 Projection (UMAP) and the Nearest Neighbor (NN) graph were initialized in this PCA space
575 using the first 20 PCs. The cells were then reclustered using the Leiden method
576 (resolution=0.5 for endothelial cells, resolution=0.3 for T cells, resolution=0.2 for fibroblasts,
577 and resolution=0.3 for cardiomyocytes) to get cell type subclusters. Differentially expressed
578 genes (wilcoxon method) for each subcluster were then used to assign cell subtype labels.
579 Subclusters representing doublets and expressing markers of multiple cell types were then
580 removed from the analysis. Normalized gene expression for differentially expressed genes and
581 genes of interest was visualized on DotPlots and UMAP plots across celltype subgroups.
582 Differential gene expression analysis (DGEA) was performed using the rank_gene_groups
583 function in Scanpy with the Wilcoxon statistical method. All gene module scores were
584 calculated using the score_genes function in Scanpy.

585 **Spatial transcriptomics data processing, integration, analysis, and visualization**

586 Spatial transcriptomics data from barcoded spatial spots from four heart sections were log-
587 normalized using the Scanpy package (1.8.1). Scanpy package was then used to select highly
588 variable genes for spatial transcriptomics data with min_disp=0.5 and max_mean=3
589 thresholds. We then performed mean centering and scaling while regressing out total UMI
590 counts, percent mitochondrial UMIs, S score, and G2M score, followed by PCA on the spot
591 gene expression matrix, and reduced the dimensions of the data to the top 20 principal
592 components. UMAP and the NN graph were initialized in this PCA space. The spots were then
593 clustered using the Leiden method with multiple values of clustering resolution. The method
594 returned spot clusters representing different tissue regions, which were then visualized on H&E
595 images as spatial transcriptomics maps for individual samples to assign anatomical regions.
596 Normalized gene expression was visualized on spatial transcriptomics maps for all tissue
597 sections. Spot clusters representing the same tissue regions were grouped into broad
598 anatomical region groups using marker genes and then used for downstream analysis.
599 Stereoscope deconvolution method implemented in the scvi-tools³⁹ package was used for
600 integration of spatial transcriptomics data with time-matched scRNA-seq data and cell type
601 prediction values for spatial transcriptomics spots were estimated for the infected heart at 7
602 dpi. DGEA for anatomical regions was performed using the rank_gene_groups function in
603 Scanpy with the Wilcoxon statistical method.

604 **Viral transcript sequencing data processing, filtering, and visualization**

605 Enriched viral transcript data were aligned to a combined mouse and reovirus type-1 Lang
606 genome for all infected samples. Viral unique molecule (UMI) counts were taken from the
607 combined expression matrices and added as metadata in the host gene expression data. Viral
608 UMI counts in empty droplets, droplets with low-quality cells (< 200 host UMI counts), droplets
609 with viable cells (≥ 200 host UMI counts) were sorted by viral UMI and visualized on a
610 histogram to filter out the cell-free ambient viral RNA enriched in the hybridization protocol.
611 Using the distribution of viral UMI counts in empty droplets, thresholds of two viral UMIs and
612 ten viral UMIs were used to identify infected cells in the heart and ileum respectively (**Supp Fig**
613 **2D**). Viral transcripts in the infected cells were then visualized on a DotPlot to determine viral
614 tropism in tissues.

615 **Gene Ontology term enrichment analysis for scRNA-seq and spatial transcriptomics**

616 Gene Ontology (GO) term enrichment analysis was performed on differentially expressed
617 genes using gseapy wrapper package⁴⁰. Differentially expressed genes (two-sided Wilcoxon
618 test, log fold-change threshold = 2.0, p-value < 10^{-4} for scRNA-seq cells, and log fold-change
619 threshold = 0.5, p-value < 10^{-2} for spatial transcriptomics spots) were selected and used for
620 GO term enrichment analysis using GO_Biological_Processes_2021 gene sets in enrichr
621 command⁴¹. The enriched GO terms of interest were selected and visualized on a BarPlot. The
622 genes associated with GO terms of interested were used to calculate module scores using
623 score_genes command in Scanpy.

624 **ACKNOWLEDGEMENTS**

625 We would like to thank Peter Schweitzer and the Cornell Genomics Center for help with single-
626 cell and spatial sequencing assays and the Cornell Bioinformatics facility for assistance with
627 bioinformatics. We also thank the members of the Parker and De Vlamincck labs for many
628 valuable discussions. This work was supported by R21AI144557 (to J.S.P. and I.D.V.), and
629 DP2AI138242 (to I.D.V.). S.T.C. was supported by the National Institutes of Health and
630 National Institute of Allergy and Infectious Diseases Award T32AI145821.

631 **AUTHOR CONTRIBUTIONS**

632 M.M., J.S.P., and I.D.V. designed the study. M.M., M.M.H., and S.T.C. performed the animal
633 experiments. M.M. and M.M.H. performed the scRNA-seq and spatial transcriptomics
634 experiments. M.M., D.W.M., and M.F.Z.W. analyzed the data. M.M., J.S.P., and I.D.V. wrote
635 the manuscript. All authors provided feedback and comments.

636 **DATA AVAILABILITY**

637 The authors declare that all sequencing data supporting the findings of this study have been
638 deposited in NCBI's Gene Expression Omnibus (GEO)⁴² with GEO series accession number

639 [GSE189636](#). Raw and processed H&E-stained tissue images and tissue-spot alignment files
640 matched to spatial transcriptomics datasets have been made publicly available on figshare
641 with identifier <https://doi.org/10.6084/m9.figshare.c.5726372>⁴³. Scripts to reproduce the
642 analysis presented in this study have been deposited on GitHub
643 (https://github.com/madhavmantri/reovirus_induced_myocarditis).

644 CONFLICTS

645 The authors declare no conflicts.

646

647

648 REFERENCES

- 649 1. Pollack, A., Kontorovich, A. R., Fuster, V. & Dec, G. W. Viral myocarditis—diagnosis, treatment
650 options, and current controversies. *Nat. Rev. Cardiol.* 2015 1211 **12**, 670–680 (2015).
- 651 2. Rose, N. R. Viral Myocarditis. *Curr. Opin. Rheumatol.* **28**, 383 (2016).
- 652 3. Yajima, T. & Knowlton, K. U. Viral myocarditis from the perspective of the virus. *Circulation* **119**,
653 2615–2624 (2009).
- 654 4. Tschöpe, C. *et al.* Myocarditis and inflammatory cardiomyopathy: current evidence and future
655 directions. *Nat. Rev. Cardiol.* **18**, 169–193 (2021).
- 656 5. Woodruff, J. F. Viral myocarditis. A review. *Am. J. Pathol.* **101**, 425 (1980).
- 657 6. Lasrado, N. & Reddy, J. An overview of the immune mechanisms of viral myocarditis. *Rev. Med.*
658 *Viro.* **30**, 1–14 (2020).
- 659 7. Sherry, B., Schoen, F. J., Wenske, E. & Fields, B. N. Derivation and characterization of an
660 efficiently myocarditic reovirus variant. *J. Virol.* **63**, 4840–4849 (1989).
- 661 8. Boehme, K. W., Lai, C. M. & Dermody, T. S. Mechanisms of reovirus bloodstream dissemination.
662 *Adv. Virus Res.* **87**, 1–35 (2013).
- 663 9. Guo, Y. *et al.* The multi-functional reovirus $\sigma 3$ protein is a virulence factor that suppresses stress
664 granule formation and is associated with myocardial injury. *PLOS Pathog.* **17**, e1009494 (2021).
- 665 10. Swirski, F. K. & Nahrendorf, M. Cardioimmunology: the immune system in cardiac homeostasis
666 and disease. *Nat. Rev. Immunol.* 2018 1812 **18**, 733–744 (2018).
- 667 11. Sherry, B., Li, X. Y., Tyler, K. L., Cullen, J. M. & Virgin, H. W. Lymphocytes protect against and
668 are not required for reovirus-induced myocarditis. *J. Virol.* **67**, 6119–6124 (1993).
- 669 12. Phillips, M. B., Dina Zita, M., Howells, M. A., Weinkopff, T. & Boehme, K. W. Lymphatic Type 1
670 Interferon Responses Are Critical for Control of Systemic Reovirus Dissemination. *J. Virol.* **95**,
671 (2021).

- 672 13. Holm, G. H. *et al.* Interferon Regulatory Factor 3 Attenuates Reovirus Myocarditis and
673 Contributes to Viral Clearance. *J. Virol.* (2010). doi:10.1128/jvi.01742-09
- 674 14. Schaum, N. *et al.* Single-cell transcriptomics of 20 mouse organs creates a Tabula Muris. *Nat.*
675 *2018* 5627727 **562**, 367–372 (2018).
- 676 15. Woudstra, L., Juffermans, L. J. M., van Rossum, A. C., Niessen, H. W. M. & Krijnen, P. A. J.
677 Infectious myocarditis: the role of the cardiac vasculature. *Heart Fail. Rev.* **23**, 583–595 (2018).
- 678 16. Chávez-Galán, L., Arenas-Del Angel, M. C., Zenteno, E., Chávez, R. & Lascurain, R. Cell death
679 mechanisms induced by cytotoxic lymphocytes. *Cell. Mol. Immunol.* **6**, 15–25 (2009).
- 680 17. Leuschner, F. *et al.* Silencing of CCR2 in myocarditis. *Eur. Heart J.* **36**, 1478–1488 (2015).
- 681 18. Miteva, K. *et al.* Mesenchymal Stromal Cells Modulate Monocytes Trafficking in Coxsackievirus
682 B3-Induced Myocarditis. *Stem Cells Transl. Med.* **6**, 1249–1261 (2017).
- 683 19. Barton, P. J. R. *et al.* Increased expression of extracellular matrix regulators TIMP1 and MMP1 in
684 deteriorating heart failure. *J. Heart Lung Transplant.* **22**, 738–744 (2003).
- 685 20. Jackson, R. *et al.* The translation of non-canonical open reading frames controls mucosal
686 immunity. *Nature* **564**, 434–438 (2018).
- 687 21. Swertfeger, D. K., Witte, D. P., Stuart, W. D., Rockman, H. A. & Harmony, J. A. K. Apolipoprotein
688 J/clusterin induction in myocarditis: A localized response gene to myocardial injury. *Am. J.*
689 *Pathol.* **148**, 1971–1983 (1996).
- 690 22. Szalay, G. *et al.* Ongoing Coxsackievirus Myocarditis Is Associated with Increased Formation
691 and Activity of Myocardial Immunoproteasomes. *Am. J. Pathol.* **168**, 1542–1552 (2006).
- 692 23. Van Der Borcht, K. *et al.* Myocarditis elicits dendritic cell and monocyte infiltration in the heart
693 and self-antigen presentation by conventional type 2 dendritic cells. *Front. Immunol.* **9**, 2714
694 (2018).
- 695 24. Duerr, G. D. *et al.* Metallothioneins 1 and 2 Modulate Inflammation and Support Remodeling in
696 Ischemic Cardiomyopathy in Mice. *Mediators Inflamm.* **2016**, (2016).
- 697 25. Bogomolovas, J. *et al.* Induction of Ankrd1 in dilated cardiomyopathy correlates with the heart
698 failure progression. *Biomed Res. Int.* **2015**, (2015).
- 699 26. Yamada, S. *et al.* Spatiotemporal single-cell analysis reveals critical roles of mechano-sensing
700 genes at the border zone in remodeling after myocardial infarction. doi:10.21203/rs.3.rs-
701 620498/v1
- 702 27. Gupta, S., Markham, D. W., Drazner, M. H. & Mammen, P. P. A. Fulminant myocarditis. *Nat.*
703 *Clin. Pract. Cardiovasc. Med.* 2008 511 **5**, 693–706 (2008).
- 704 28. Lindner, D. *et al.* Association of Cardiac Infection With SARS-CoV-2 in Confirmed COVID-19
705 Autopsy Cases. *JAMA Cardiol.* **5**, 1281–1285 (2020).
- 706 29. Bräuning, H. *et al.* Cardiac SARS-CoV-2 infection is associated with pro-inflammatory
707 transcriptomic alterations within the heart. *Cardiovasc. Res.* (2021). doi:10.1093/CVR/CVAB322

- 708 30. Lasrado, N., Borchering, N., Arumugam, R., Starr, T. K. & Reddy, J. Dissecting the Cellular
709 Landscape and Transcriptome Network in Viral Myocarditis by Single-Cell RNA Sequencing.
710 *bioRxiv* 2021.05.16.444367 (2021). doi:10.1101/2021.05.16.444367
- 711 31. Mantri, M. & Scuderi, G. J. Spatiotemporal single-cell RNA sequencing of developing chicken
712 hearts identifies interplay between cellular differentiation and morphogenesis.
713 *Github:chicken_heart* (2020). doi:<https://doi.org/10.5281/zenodo.4517120>
- 714 32. Asp, M. *et al.* A Spatiotemporal Organ-Wide Gene Expression and Cell Atlas of the Developing
715 Human Heart. *Cell* **179**, 1647-1660.e19 (2019).
- 716 33. Kuppe, C. *et al.* Spatial multi-omic map of human myocardial infarction. *bioRxiv*
717 2020.12.08.411686 (2020). doi:10.1101/2020.12.08.411686
- 718 34. Baty, C. J. & Sherry, B. Cytopathogenic effect in cardiac myocytes but not in cardiac fibroblasts
719 is correlated with reovirus-induced acute myocarditis. *J. Virol.* **67**, 6295–6298 (1993).
- 720 35. Stewart, M. J., Blum, M. A. & Sherry, B. PKR's protective role in viral myocarditis. *Virology* **314**,
721 92–100 (2003).
- 722 36. Miyamoto, S. D. *et al.* Cardiac Cell-specific Apoptotic and Cytokine Responses to Reovirus
723 Infection: Determinants of Myocarditic Phenotype. *J. Card. Fail.* **15**, 529–539 (2009).
- 724 37. Stewart, M. J., Smoak, K., Blum, M. A. & Sherry, B. Basal and Reovirus-Induced Beta Interferon
725 (IFN- β) and IFN- β -Stimulated Gene Expression Are Cell Type Specific in the Cardiac Protective
726 Response. *J. Virol.* **79**, 2979–2987 (2005).
- 727 38. Wolf, F. A., Angerer, P. & Theis, F. J. SCANPY: Large-scale single-cell gene expression data
728 analysis. *Genome Biol.* **19**, 1–5 (2018).
- 729 39. Gayoso, A. *et al.* scvi-tools: a library for deep probabilistic analysis of single-cell omics data.
730 *bioRxiv* 2021.04.28.441833 (2021). doi:10.1101/2021.04.28.441833
- 731 40. Subramanian, A. *et al.* Gene set enrichment analysis: A knowledge-based approach for
732 interpreting genome-wide expression profiles. *Proc. Natl. Acad. Sci.* **102**, 15545–15550 (2005).
- 733 41. Xie, Z. *et al.* Gene Set Knowledge Discovery with Enrichr. *Curr. Protoc.* **1**, e90 (2021).
- 734 42. Edgar, R. Gene Expression Omnibus: NCBI gene expression and hybridization array data
735 repository. *Nucleic Acids Res.* (2002). doi:10.1093/nar/30.1.207
- 736 43. Mantri, M. Reovirus-induced-myocarditis. (2021).
737 doi:<https://doi.org/10.6084/m9.figshare.c.5726372>